

van der Waals Epitaxy of $\text{Co}_{10-x}\text{Zn}_{10-y}\text{Mn}_{x+y}$ Thin Films: Chemical Composition Engineering and Magnetic Properties

Anna Kúkolová,* Simon Escobar Steinvall, Rajrupa Paul, Jean-Baptiste Leran, Ping Che, Mohammad Hamdi, Andrea Mucchietto, Dirk Grundler,* and Anna Fontcuberta i Morral*



Cite This: <https://doi.org/10.1021/acs.jpcc.1c00452>



Read Online

ACCESS |



Metrics & More



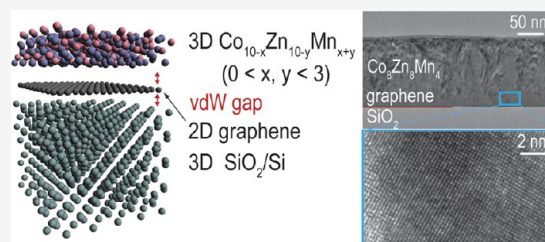
Article Recommendations



Supporting Information

ABSTRACT: Topologically protected magnetic skyrmions have raised interest for future spintronics applications. One of the main challenges is the synthesis of room temperature skyrmion-hosting materials that are compatible with thin-film technology. We present an approach to produce strain-free epitaxial thin films of $\text{Co}_{10-x}\text{Zn}_{10-y}\text{Mn}_{x+y}$ using molecular beam epitaxy. Bulk $\text{Co}_{10-x}\text{Zn}_{10-y}\text{Mn}_{x+y}$ is known to host skyrmions at room temperature for specific composition ratios. Our substrate consists of graphene on oxidized silicon. The van der Waals interactions of the grown material with graphene prevents covalent bonding and corresponding strain.

We show how defects in the graphene foster nucleation that results in three different kinds of morphologies: islands, columns, and merged films. Susceptibility measurements suggest a phase transition close to room temperature. We detect up to three spin waves resonances suggesting relatively low magnetic damping. This growth technique opens a new route for the integration of complex alloys and skyrmionic device concepts with silicon electronics.



INTRODUCTION

Bloch type skyrmions have been observed in a variety of materials with regard to their conduction type and shape. The first experimental proof of a skyrmion lattice (SkX) came from the bulk single-crystalline metal MnSi with B20 crystal structure.¹ It was confirmed by small angle neutron scattering (SANS) experiments and topological Hall effect (THE) that the SkX in MnSi occurs below a critical temperature T_c of 30 K.^{2–4} A further skyrmion-hosting bulk metallic compound is FeGe with $T_c = 283$ K.⁵ Skyrmions were also observed in bulk semimetals $\text{Fe}_{1-x}\text{Co}_x\text{Si}^6$ and the insulator Cu_2OSeO_3 ,⁷ both with SkX below 36 and 58 K, respectively. So far, the only room temperature Bloch SkX-hosting compound is metallic $\text{Co}_8\text{Zn}_8\text{Mn}_4$.⁸

In thinned bulk samples, an extended skyrmion phase was observed by Lorentz transmission electron microscopy (LTEM) in MnSi⁹ and in $\text{Co}_{8.5}\text{Zn}_{7.5}\text{Mn}_4$.¹⁰ In these studies, membranes were prepared by ion milling. Similar to that in membranes, the presence of extended skyrmion phase was suggested also for epitaxially grown thin films of MnSi/Si(111),¹¹ $\text{Mn}_{1-x}\text{Fe}_x\text{Si}/\text{Si}(111)$,¹² and FeGe/Si(111).^{5,13} SkX at lower field and smaller SkX lattice constants were implied from phase diagrams measured on $\text{Fe}_{0.75}\text{Co}_{0.25}\text{Si}^{14}$ and MnSi nanowires.¹⁵ Still, strain-induced modifications of the magnetic and electronic properties of epilayers are controversial. While strain has led to the stabilization of SkX at higher critical temperature in $\text{Fe}_{1-x}\text{Co}_x\text{Si}/\text{Si}(111)$ epilayers by distortion of the cubic structure into a rhombohedral structure,¹⁶ in MnSi/Si(111), no skyrmions were observed in the strained epilayers by LTEM,

although they still exhibited skyrmion-like characteristics when investigated through THE.¹⁷

Ternary $\text{Co}_{10-x}\text{Zn}_{10-y}\text{Mn}_{x+y}$ alloys with β -Mn structure (cubic chiral space group $P4_132$ and $P4_332$) were found to exhibit triangular SkX in a wide range of temperatures from 210 to 470 K in bulk crystals.⁸ The Curie temperature T_c was tuned by the composition ratio between Co, Zn, and Mn. In particular, a high Mn concentration lowered T_c . Figure 1a illustrates the β -Mn unit cell with its 20 atoms. We indicate the two nonequivalent symmetry sites: the 3-fold symmetry 8c sites and the 2-fold symmetry 12d sites. Bocarsly¹⁸ and Nakajima¹⁹ showed that in $\text{Co}_{10-x}\text{Zn}_{10-y}\text{Mn}_{x+y}$, 8c and 12d sites were preferentially occupied by Co and Zn, respectively. Substituting Co and Zn with Mn, Mn atoms preferred to occupy 12d sites. Above approximately $x + y > 3$, Mn started to occupy 8c sites too.¹⁸ Other configurations, like square or distorted SkX, have been observed at low temperatures when the material was cooled in an applied magnetic field.²⁰ $\text{Co}_{10-x}\text{Zn}_{10-y}\text{Mn}_{x+y}$ thin films grown on substrates have not yet been reported.

In this paper, we show the growth of $\text{Co}_{10-x}\text{Zn}_{10-y}\text{Mn}_{x+y}$ on graphene by molecular beam epitaxy (MBE). Growth of thin films on a van der Waals material such as graphene (Figure 1b) is

Received: January 18, 2021

Revised: April 15, 2021

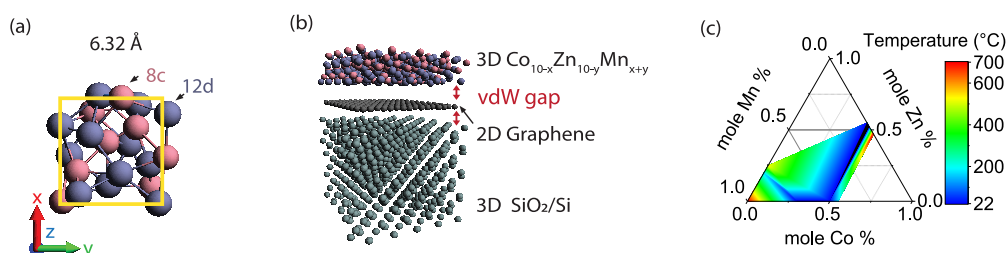


Figure 1. (a) β -Mn cubic crystal structure with the unit cell containing 20 atoms. 8c sites with the 3-fold symmetry are preferentially filled with Co and 12d sites with the 2-fold symmetry are filled with Zn in the parent compound $\text{Co}_8\text{Zn}_{12}$. The lattice parameter of the unit cell is 6.32 Å. (b) Schematic van der Waals epitaxy of $\text{Co}_{10-x}\text{Zn}_{10-y}\text{Mn}_{x+y}$ on graphene on SiO_2/Si with vdW gaps at the interfaces with the graphene. (c) Ternary phase diagram of Co–Zn–Mn. β -Mn phase depicted in color. The color code represents the minimal temperature required for the β -Mn phase synthesis.

known as van der Waals (vdW) epitaxy.^{21–24} Here, the thin film is bound to the substrate by van der Waals interactions. This relaxes the epitaxial requirements with respect to matching lattice constants and thermal expansion coefficient.²⁵ Another advantage is that the films are relatively easy to transfer to an arbitrary substrate after growth. The use of graphene as an underlayer renders nucleation challenging as a consequence of the weak interaction with the substrate. In the synthesis of complex alloys such as $\text{Co}_{10-x}\text{Zn}_{10-y}\text{Mn}_{x+y}$, an additional challenge arises in finding the right parameter space to engineer the alloy composition. For this, the sticking and desorption parameters of Co, Zn, and Mn as well as the phase diagram need to be considered. Table 1 summarizes the adatom-graphene

layer-by-layer fashion as compared to Co or Mn. Thin-film synthesis on graphene was shown to be strongly affected by the presence of defects.²⁷ While the lack of dangling bonds on pristine graphene rendered the chemisorption difficult, defects initiated the growth.

Figure 1c presents the ternary phase diagram of Co–Zn–Mn extrapolated from the binary phase diagrams of Co–Zn, Zn–Mn and Mn–Co.^{28–30} The colored region presents the stable β -Mn phase; the color code represents the minimal growth temperature. We are interested in the alloys with $0 < x, y < 6$ previously reported for bulk crystals to host skyrmions, especially in $\text{Co}_8\text{Zn}_8\text{Mn}_4$ hosting skyrmions at room temperature.⁸

Table 1. Adatom–Graphene Distance, Adsorption, and Migration Barrier Energies for Co, Zn, and Mn Elements on Graphene Extracted from DFT Calculations^a

Atom	Adatom-graphene distance (Å)	Adsorption energy (eV)	Migration energy (eV)
Co	1.42	3.64	0.77
Zn	3.02	0.13	0.02
Mn	1.38	3.82	1.26

^aValues from ref 26.

distance, adsorption, and migration energy for Co, Zn, and Mn. These values were previously calculated by density functional theory (DFT) by Nakada and Ishii.²⁶ Co and Mn have relatively high adsorption energy compared to Zn on graphene, which is what makes them nucleation-initiating elements. The migration energy barrier is very low for Zn, high for Co, and the highest for Mn. This suggests Zn thin films are more likely to grow in a

EXPERIMENTAL SECTION

$\text{Co}_{10-x}\text{Zn}_{10-y}\text{Mn}_{x+y}$ thin films were grown in a GenXplor Veeco ultrahigh vacuum (UHV) molecular beam epitaxy system (MBE) with a base pressure of 3×10^{-10} mTorr. The substrates consisted of commercially available graphene deposited on oxidized Si (100) wafers (300 nm of SiO_2). The 4 in. wafers were diced into 15×15 mm² chips. Upon introduction to the MBE system and prior to deposition, the substrates were cleaned through a two-step degassing process at 150 °C for 1.5 h and 450 °C for 2 h in HV respectively. The substrate temperature^a was varied between 180 and 270 °C, as measured by a thermocouple. We varied the Co:Zn:Mn flux ratios to engineer the alloy composition and find the growth conditions for $1 \leq x, y \leq 3$. Overall, the beam equivalent pressures of Co, Zn, and Mn were varied between 1×10^{-8} and 5×10^{-7} mTorr as measured by a beam flux monitor. To understand the growth mechanism, we performed growth time series ranging from 5 min to 3 h.

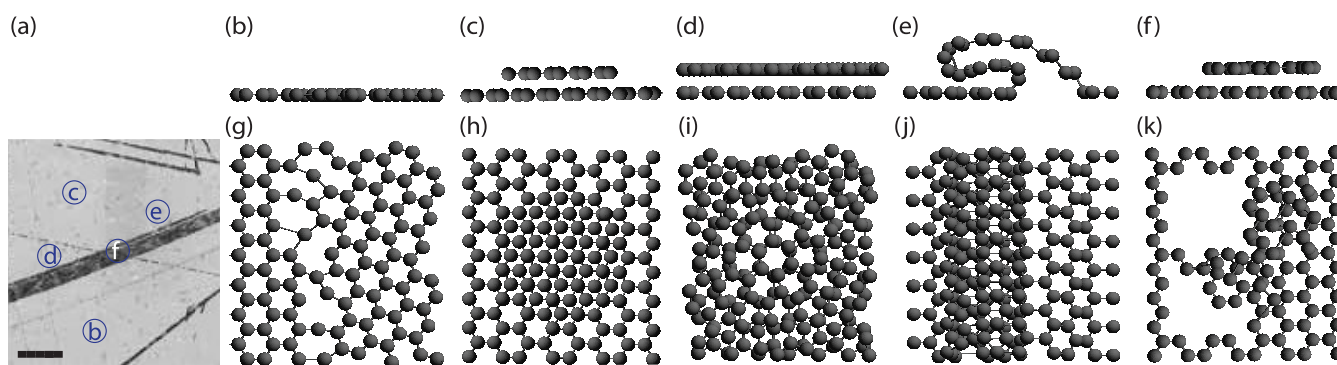


Figure 2. (a) SEM top view of graphene on a SiO_2/Si substrate. We observe the following defects in the graphene layer which we sketch in separate panels on the right: (b, g) grain boundary (GB) with side and top view sketch, respectively; (c, h) the bilayer graphene (BLG); (d, i) the double-layer (DLG); (e, j) the graphene wrinkle (GW); (f, k) the released graphene and partial DLG formation in. Scale bar in (a) 20 μm .

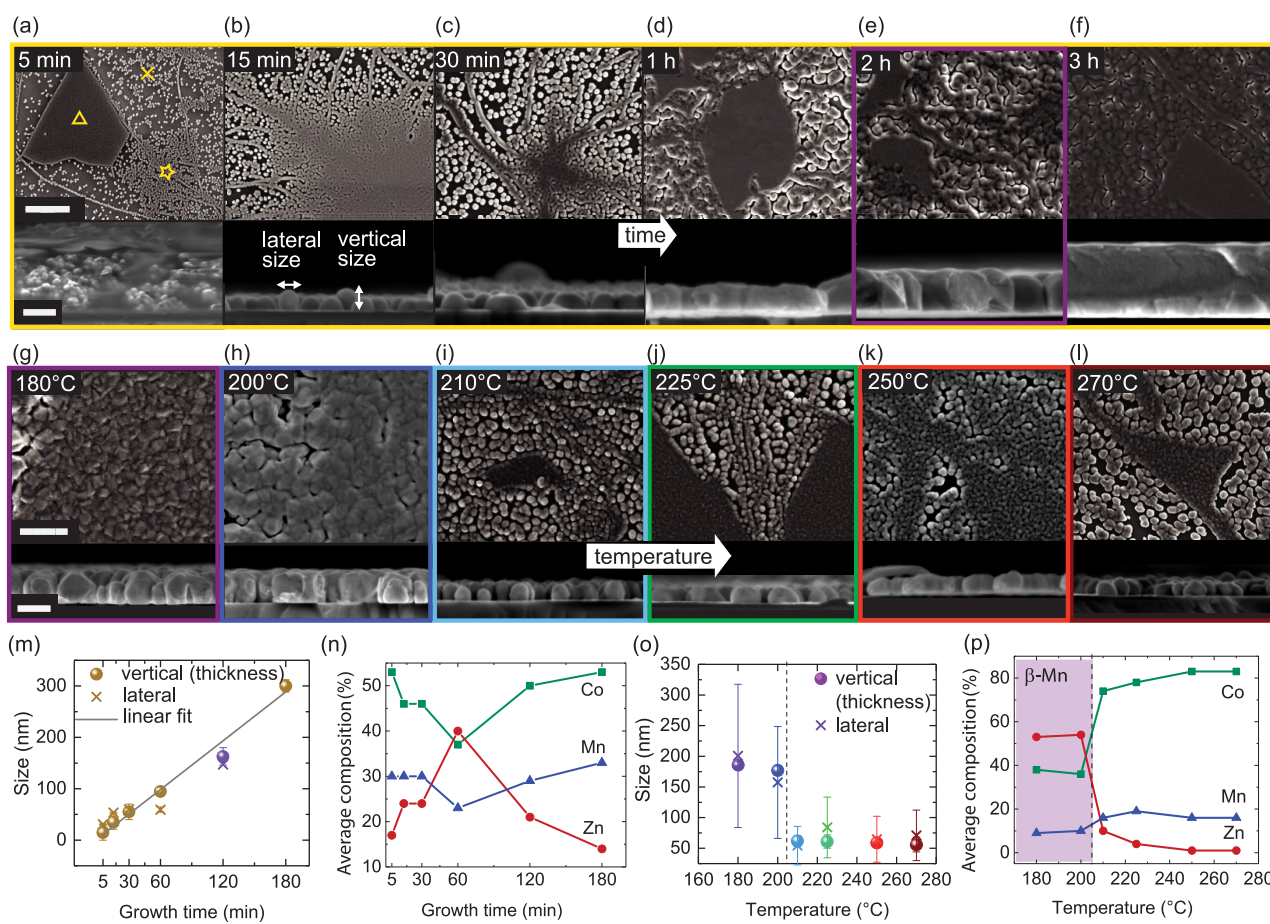


Figure 3. (a–f) Time series of CoZnMn film grown at manipulator temperature $T = 180^\circ\text{C}$. SEM top and side view micrographs for (a) 5 min (b) 15 min, (c) 30 min, (d) 1 h, (e) 2 h, and (f) 3 h. We observe three different regions due to the graphene quality depicted in part a: nucleation on disattached graphene (Δ), BLG (\star) and SLG (\times). (g–l) Temperature series of CoZnMn growth for 2 h. SEM top and side micrographs for substrate temperature (g) 180°C , (h) 200°C , (i) 210°C , (j) 225°C , (k) 250°C , and (l) 270°C . (m) The time evolution of film thickness follows a linear trend, the lateral growth is faster for depositions shorter than 1 h. (n) The average composition for Co (green rectangle), Zn (red circle), and Mn (blue triangle) as a function of growth time. Zn concentration first increases with film coverage, then it decreases as the film roughness decreases by forming a merged film. (o) The temperature dependence of film thickness exhibits an abrupt change for $T > 200^\circ\text{C}$ when the thickness drops from 183 to 60 nm. The lateral growth follows the same trend. (p) The average composition for Co (green rectangle), Zn (red circle), and Mn (blue triangle) as a function of substrate temperature. The zinc concentration abruptly decreases for T above 200°C , attributed to an increased Zn desorption for high temperature. Scale bars: (parts a–f) top view 500 nm, side view 100 nm; (parts g–l) top view 500 nm, side view 200 nm.

After the growth, the sample morphology was imaged using the field emission scanning electron microscope (FE-SEM) Zeiss Merlin with the accelerating voltage of 3 kV. The average composition was analyzed through the electron X-ray dispersion spectroscopy (EDS) in Zeiss Merlin FE-SEM (5 kV). A more detailed characterization of the composition and microstructure was performed on selected samples by transmission electron microscope (TEM) FEI Tecnai Osiris and Talos, scanning transmission electron microscopy (STEM, 200 kV), and electron X-ray dispersion spectroscopy STEM-EDS. For this, thin lamellae were produced using focused-ion beam FIB-SEM Zeiss NVision 40. The crystal phase was also measured with the grazing incidence X-ray diffractometer (GIXRD) Panalytical Empyrean. The static magnetization M was measured using a Quantum Design's superconducting quantum interference device (SQUID) magnetometer. The magnetic hysteresis loops were measured at 5 and 300 K in the range of applied fields $\mu_0 H$ of ± 500 mT. Temperature dependent magnetization curves were obtained via Quantum Design's vibrating sample magnetometer (VSM) with cooling in a field of 5 mT from 350 to 5 K. The dynamic susceptibility was acquired with Quantum

Design's alternating current magnetic susceptometer (ACMS) during cooling in 20 mT from 350 to 5 K, using a drive field of 0.1 mT at a frequency of 10 kHz. The fields were applied in the plane of the thin films. We studied the spin-wave resonances at room temperature using Brillouin light scattering (BLS) spectroscopy in the frequency range from 3.5 to 12 GHz for applied in-plane fields ranging from 20 to 250 mT.

RESULTS AND DISCUSSION

Morphology, Structure, and Composition. Figure 2a corresponds to a SEM image of a graphene layer prior to the growth. The contrast in the image is attributed to different kinds of defects. Figure 2b–k illustrates the different defects which we identified in the graphene. The graphene was grown by CVD on a Cu foil and then transferred to the SiO_2/Si substrate. Some defects are due to the polycrystallinity of the copper substrate, such as grain boundaries (GBs) (a, b, g). At the junction of GBs, bilayer graphene (BLG) is observed (dark lines in a, c, h). With an arbitrary rotation of two stacked single-layer graphene (SLG) layers, we obtain double-layer graphene (DLG) (a, d, i). Graphene wrinkles (GWs) are related to the different thermal

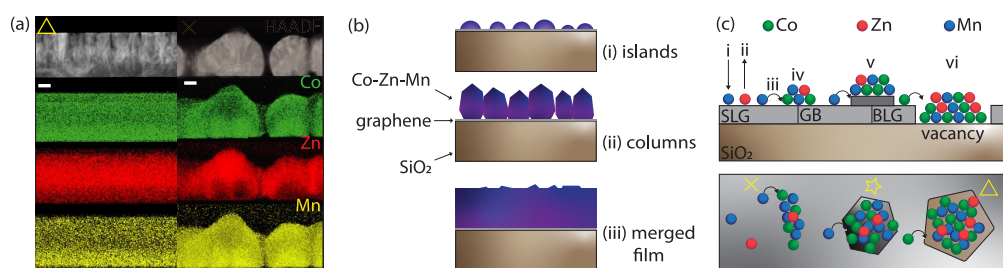


Figure 4. (a) STEM-EDS on a merged film (Δ) and on the islands (\times) of $\text{Co}_8\text{Zn}_8\text{Mn}_4$. Scale bar 20 nm. (b) Three types of observed morphology: islands, columns and merged film. (c) The illustration of processes observed during the time series: (i) adsorption, (ii) desorption, (iii) surface diffusion leading to island nucleation on (\times) SLG and (iv) GBs. The columns (\star) are observed on (v) BLG and GWs. The merged film (Δ) grows on DLG and (vi) graphene vacancies.

expansion between the graphene and the copper substrate (a, e, j). Further defects are assumed to occur during the transfer to the new substrate (a, f, k). We identified the defects by Raman spectroscopy (see Figure S1 in Supporting Information).

We turn now to the growth of $\text{Co}_{10-x}\text{Zn}_{10-y}\text{Mn}_{x+y}$ on these substrates. We start with a time series to understand what kind of surface features favor the initiation of the thin films. The Co, Zn, and Mn beam equivalent pressures were set to 2×10^{-7} , 4×10^{-8} , and 4×10^{-7} mTorr, respectively. These BEP values were chosen by taking into account the growth rate calibration of the individual elements. The substrate temperature was set to $T = 180$ °C. These conditions led to the average composition ratio 37:40:23 (Co:Zn:Mn) for 60 min deposition as determined by STEM-EDS. In the following, we refer to this sample as $\text{Co}_8\text{Zn}_8\text{Mn}_4$, i.e., its closest nominal composition. Figure 3a–f shows the top and side view SEM micrographs for growth process ranging from 5 min to 3 h. The 5 min long deposition provided island growth, mostly on the wrinkles and grain boundaries of graphene. At this stage the islands exhibited a height around 15 ± 15 nm (vertical size) and an average diameter of 31 ± 9 nm (lateral size). We distinguish three different regions: merged film, columnar growth, and islands denoted as Δ , \star , and \times , respectively, which we attribute to the different graphene morphologies (Figure 3a). Different morphologies were also observed for Au on different graphene surfaces.^{31,32} After a 15 min long growth, the vertical size of the islands increased to 35 ± 14 nm and the lateral growth to 53 ± 8 nm indicating that the lateral growth is faster than vertical. After a 1 h long deposition, we observed almost full coverage with coalescence of regions Δ (Figure 3d). Figure 3e,f shows 2 and 3 h long deposition processes where the film thickness increased from 163 ± 17 to 300 ± 12 nm. The evolution of the thickness and island lateral size is summarized in Figure 3m. The film thickness increased linearly as a function of deposition time with a growth rate of 98 ± 3 nm/h. For deposition periods smaller than 1 h, the lateral growth was faster than vertical one. For a 1 h long deposition process, almost full coverage of the graphene was achieved. For a deposition beyond 1 h, the grains merged and the film grew vertically. From the literature, we know that Mn³³ and Co³⁴ have the tendency to follow the Volmer–Weber growth, consistent with the islands observed here. We find that the island density increases with the coverage before merging into a thin film.^{35,36}

The average composition of these films as a function of time was determined through SEM-EDS and is shown in Figure 3n. We find the cobalt and manganese concentration is highest during the initial stage of the thin film formation. The zinc concentration takes its maximum value of 40% after 1 h of

deposition, when full coverage is achieved. The zinc concentration decreases to 10% as the deposition time reaches 3 h. These results suggest that the adsorption rates of Co, Zn, and Mn atoms depend also on the surface area change comprising the effect of coverage and film roughness for a given substrate temperature.

Below, we discuss the effect of substrate temperature on the growth morphology. Top and side view micrographs of samples after a deposition period of 2 h are shown in Figure 3g–l. From left to right, T varied from 180 to 270 °C. The Co, Mn, and Zn partial pressures were set to 3×10^{-8} , 8×10^{-9} , and 4×10^{-7} mTorr, respectively. The vertical (thickness) and lateral sizes of grains are summarized in Figure 3o. The films deposited at 180 and 200 °C show very similar morphology and an average thickness of 183 ± 3 nm with full coverage (Figure 3g,h). The coverage and the grain size drastically change as we increase T beyond 200 °C (Figure 3i): the vertical grain size decreases to about 60 ± 2 nm and remains at this value for 225, 250, and 270 °C (Figure 3j–l). The coverage and grain shape stay also the same for temperatures above 215 °C. Figure 3p reports the average composition as a function of temperature. The average composition remains at a ratio Co:Zn:Mn = 39:51:10 at 180 and 200 °C. For higher temperature, we observe a strong reduction in zinc concentration and an increase in Co. We attribute this to the desorption of Zn, which depends much more on temperature than Co.²⁶

We studied the composition variations within the thin films with STEM-EDS, in that, we explored thin lamellae prepared by FIB. Figure 4a shows the high-angle annular dark-field (HAADF) images and the composition maps measured for sample $\text{Co}_8\text{Zn}_8\text{Mn}_4$ grown at $T = 180$ °C for 1 h (compare Figure 3d). The images show a merged film (left) and islands (right). Both were acquired on the same sample. HAADF images indicate a heterogeneity from bottom to top. The initial stages of growth (bottom parts) are rich in Co and Mn. The Zn incorporation increases for a thickness larger than 35 nm. These observations are consistent for a merged film and islands.

We attribute the variation in composition to the different adsorption and migration energies for Co, Zn, and Mn (Table 1). This is consistent with nucleation starting with Co and Mn due to their high adsorption energy and low mobility. Zn concentration is expected to increase for the following two cases: (i) graphene is fully covered by Co or Mn and (ii) rough surfaces, which effectively lower the Zn surface mobility in a similar fashion to what has been observed before.³⁷ We summarize our findings through the illustrations in Figure 4b,c. In the time evolution of the thin films, we observe (Figure 4b): (i) islands, (ii) columns, and (iii) merged films. Islands are

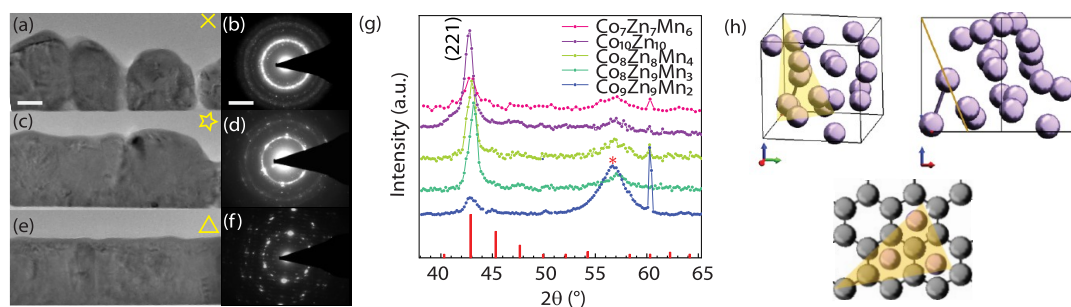


Figure 5. TEM BF and corresponding SAED patterns of $\text{Co}_8\text{Zn}_8\text{Mn}_4$. (a) columns (X) with (b) the ring diffraction pattern corresponding to nanocrystallites. (c) Granular film and (d) the diffraction pattern with preferential grain orientation around $[2-56]$ zone axis. (e) Merged film and (f) the spot diffraction pattern corresponding to a β -Mn single crystal at $[256]$ zone axis. Scale bars: (parts a, c, and e) 100 nm; (parts b, d, and f) 5 nm^{-1} . (g) X-ray diffraction of $\text{Co}_{10-x}\text{Zn}_{10-y}\text{Mn}_{x+y}$ layers with different stoichiometry showing the preferential crystalline orientation in the (221) direction, the broad peak at 57° corresponds to the stage. (h) Atomic distribution of atoms in the 221 plane as well as the matching with the graphene distribution.

obtained in regions with sparse nucleation points and grow freely in lateral direction. Columnar growth is found in regions with dense nucleation. Their lateral growth is limited, leading to preferential vertical growth. A merged film results from the coalescence of islands and columns. A schematic representation of the model is shown in Figure 4c. Graphene is indicated in gray on top of SiO_2 (brown). The different defects of graphene are indicated by labels: SLG, BLG, and GB (compare Figure 2). The following processes contribute to the thin film formation: (i) adsorption, (ii) desorption, (iii) surface diffusion, and (iv–vi) nucleation. Islands (X) nucleate on pristine SLG and GBs. The columns (★) are observed on BLG and GWs. The merged film (Δ) grows on DLG and graphene vacancies.

The microstructure and crystal phase of the $\text{Co}_8\text{Zn}_8\text{Mn}_4$ sample were investigated by bright field (BF) imaging and selected area electron diffraction (SAED) in TEM and GIXRD. Figure 5a–f shows BF and SAED micrographs for the islands, columns, and merged thin film regions. Each region exhibited a different degree of crystallinity. Figure 5a,b correspond to islands (X). We do not observe any misfit dislocations on the BF micrographs which is consistent with the vdW epitaxial growth (HRTEM image in Figure S2 in Supporting Information). SAED indicates the grains are composed of randomly oriented nanocrystals due to the observed ring pattern. In Figure 5c,d, the columns (★) exhibit a nanocrystalline pattern with a preferential grain orientation. For the merged film (Δ), we see a single-crystalline hexagonal pattern (using a small SA aperture to isolate a small region) in Figure 5e,f. This leads to the conclusion that the grain size increases as the islands merge into a film. We attribute this to the rearrangement of atoms toward a more energetically stable state. The crystal phase was investigated from electron diffractograms (Figure 5b,d,f) and GIXRD (Figure 5g). We used the JEMS software for comparison of SAED patterns with β -Mn $\text{Co}_8\text{Zn}_{12}$. The obtained crystal phase is in agreement with the β -Mn pattern for the $[2-56]$ zone axis orientation. For more details, see Figure S3 in Supporting Information. Figure 5g shows the comparison of the GIXRD of $\text{Co}_{10-x}\text{Zn}_{10-y}\text{Mn}_{x+y}$ films of different stoichiometry. The main peak at 42.9° corresponds to the β -Mn (221) direction. The broad peak at 57° is the signal from the stage. We sketch the atomic distribution of atoms in the $[221]$ plane in Figure 5h on top. The bottom sketch represents the orientation of the three β -Mn atoms of $[221]$ plane with respect to the graphene lattice. The preferential orientation of the grains and the crystallo-

graphic relation with the graphene underneath reveals the van der Waals epitaxy nature of the thin film formation.

Magnetic Characterization. In this section, we discuss static and dynamic magnetic properties of samples with nominal compositions $\text{Co}_{10}\text{Zn}_{10}$, $\text{Co}_9\text{Zn}_9\text{Mn}_2$, $\text{Co}_8\text{Zn}_9\text{Mn}_3$, $\text{Co}_8\text{Zn}_8\text{Mn}_4$, and $\text{Co}_7\text{Zn}_7\text{Mn}_6$ acquired with SQUID, ACMS, and BLS. These samples were grown at a substrate temperature of 180°C for 2 h as described in the previous section. In Table 2, the targeted

Table 2. $\text{Co}_{10-x}\text{Zn}_{10-y}\text{Mn}_{x+y}$ Thin Films Grown on Graphene at $T = 180^\circ\text{C}$ for 2 h Targeting at Optimized Composition Ratios^a

Material	$T_{C_{\text{expected}}}$ (K)	Thickness (nm)	Avg composition Co:Zn:Mn
$\text{Co}_{10}\text{Zn}_{10}$	470	34 ± 2	10:10:0
$\text{Co}_9\text{Zn}_9\text{Mn}_2$	415	123 ± 6	8.8:8.6:2.6
$\text{Co}_8\text{Zn}_9\text{Mn}_3$	340	123 ± 3	8.4:8.8:2.8
$\text{Co}_8\text{Zn}_8\text{Mn}_4$	300	97 ± 4	7.4:8: 4.6
$\text{Co}_7\text{Zn}_7\text{Mn}_6$	210	90 ± 4	7.4:7.2:5.4

^aThe thicknesses were measured on lamellae by TEM. The average composition was measured by STEM-EDS.

nominal composition and expected critical temperatures are summarized in the two left columns. The film thicknesses ranged from 34 to 123 nm (third column). In the right column, we report the average composition ratio measured by STEM-EDS.

Magnetic hysteresis curves $M(H)$ were measured via SQUID. We extracted saturation magnetization values M_{sat} at $T = 5 \text{ K}$ and $T = 300 \text{ K}$ for the five samples as shown in Figure 6a. From left to right, the Mn content increases. The average saturation magnetization M_{sat} was extracted from the second and fourth quadrant of the hysteresis curves at $+500$ and -500 mT . The experimental data are compared with the literature data for bulk Co–Zn–Mn samples^{18,38} with the compositions corresponding to the targeted values. M_{sat} values for $T = 5$ and 300 K follow a nonmonotonous trend as a function of Mn concentration. Our thin-film M_{sat} values are consistent with literature values of bulk materials for large Mn content in $\text{Co}_7\text{Zn}_7\text{Mn}_6$. M_{sat} values of thin films are three times smaller than bulk values for stoichiometries with small x, y values.

Figure 6b shows the coercive fields $\mu_0 H_c$ extracted from hysteresis curves of the same samples. $\text{Co}_{10}\text{Zn}_{10}$, $\text{Co}_8\text{Zn}_8\text{Mn}_4$, and $\text{Co}_7\text{Zn}_7\text{Mn}_6$ exhibit $\mu_0 H_c$ values of up to $80 \pm 2 \text{ mT}$ at $T = 5 \text{ K}$, while $\text{Co}_9\text{Zn}_9\text{Mn}_2$ and $\text{Co}_8\text{Zn}_9\text{Mn}_3$ exhibit values of $24 \pm 2 \text{ mT}$. The comparison with the literature data for bulk Co–Zn–

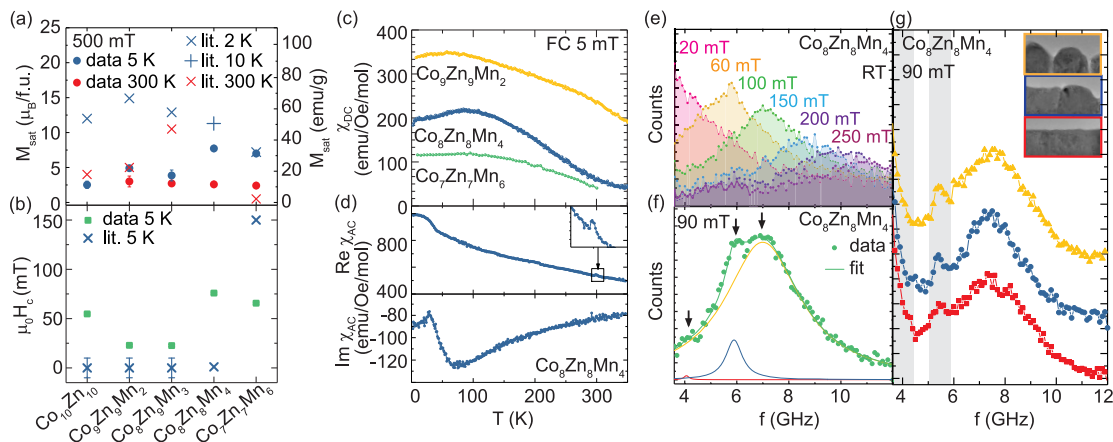


Figure 6. (a) Saturation magnetization M_{sat} as a function of CoZnMn composition for in-plane fields at 5 K (blue) and 300 K (red) extracted as the average value from the magnetization values taken at +500 and −500 mT. At 300 K, a diamagnetic contribution was subtracted from the hysteresis curves. The inset contains the literature data at 2 K,¹⁸ 10 K,³⁸ and 300 K.¹⁸ (b) Coercive field $\mu_0 H_c$ as a function of composition at $T = 5$ K given as the average value of the coercive fields extracted from the second and fourth quadrant of the hysteresis loop. Comparison with the literature data for bulk samples (blue cross) suggests, in general, higher coercive values for thin films with the exception of $\text{Co}_7\text{Zn}_7\text{Mn}_6$. (c) Temperature dependent magnetization measurement during the FC at 5 mT in-plane field. Comparison for $\text{Co}_9\text{Zn}_9\text{Mn}_2$ (yellow), $\text{Co}_8\text{Zn}_8\text{Mn}_4$ (blue), and $\text{Co}_7\text{Zn}_7\text{Mn}_6$ (green). (d) AC susceptibility of $\text{Co}_8\text{Zn}_8\text{Mn}_4$ during the FC with a DC field of 20 mT. (e) BLS spectrum of the thermal magnon acquired at $T = 300$ K in the varying in-plane field from 20 to 250 mT in $\text{Co}_8\text{Zn}_8\text{Mn}_4$. (f) Refined measurement at 90 mT and deconvolution of the peak into three possible modes. (g) BLS spectra attributed to columns (yellow), granular (blue), and merged (red) film of $\text{Co}_8\text{Zn}_8\text{Mn}_4$. They were measured at RT and 90 mT after performing detailed AFM measurements (see Figure S5 in Supporting Information). The spectra are plotted with an offset. The greyed areas correspond to peaks due to elastically scattered laser light.

Mn samples¹⁸ shows that thin-film and bulk data have a common trend: the coercive field is overall higher for large Mn content.

The temperature dependent susceptibility $\chi(T)$ was successfully acquired by VSM for $\text{Co}_9\text{Zn}_9\text{Mn}_2$, $\text{Co}_8\text{Zn}_8\text{Mn}_4$, and $\text{Co}_7\text{Zn}_7\text{Mn}_6$. Their field cooling (FC) molar susceptibilities χ_{DC} at an external field of 5 mT are displayed in Figure 6c. We observe that, depending on the Mn content, the DC susceptibilities first increase with temperature slightly and then decrease. Such temperature dependencies are in qualitative agreement with magnetization measurements reported for bulk samples with different Mn contents.^{8,18,39} In refs 19 and 40–43, the low-temperature variation of the susceptibility was argued to indicate the existence of a spin-glass state. The variations in Figure 6c could hint also at the occurrence of an antiferromagnetic phase in the samples at low temperatures. The three samples show a smeared phase transition in Figure 6c at high temperatures which might be explained by the two-sublattice model. It has been argued by Bocarsly et al.¹⁸ that cobalt develops a small ferromagnetic moment on 8c sites in the unit cell, and single Mn atoms exhibit large and dynamically distorted moments on 12d sites which fluctuate below T_c . Consistent with the two-sublattice model, we observe that the transition becomes more and more smeared the larger the Mn content.

The molar AC susceptibilities χ_{AC} were measured by ACMS in the temperature range 5–350 K during field cooling with a DC field of 20 mT. Here, we report on sample $\text{Co}_8\text{Zn}_8\text{Mn}_4$ providing us with a sufficient signal-to-noise ratio. The real and imaginary part of the susceptibility $\text{Re } \chi_{\text{AC}}$ and $\text{Im } \chi_{\text{AC}}$ are displayed in Figure 6d. In $\text{Im } \chi_{\text{AC}}$, we observe a peak near 30 K, consistent with the previous reports about the spin-glass state at the lowest temperature. Also the real part varies near 30 K. In contrast to the bulk crystals,⁴² $\text{Re } \chi_{\text{AC}}$ does not take a local minimum at the lowest temperature but a maximum. We note that the local minimum in $\text{Re } \chi_{\text{AC}}$ reported for bulk materials

depended critically on the applied field value. The open question that will be evaluated in further studies is if these materials behave distinctly as thin films compared to the bulk form. In $\text{Re } \chi_{\text{AC}}$, a further small feature indicates a transition at 300 K. This temperature agrees with the transition temperature to the skyrmion phase expected from the bulk material (Table 2). In $\text{Im } \chi_{\text{AC}}$, we were not able to resolve a specific signature.

We performed BLS spectroscopy on samples $\text{Co}_8\text{Zn}_8\text{Mn}_4$, $\text{Co}_7\text{Zn}_7\text{Mn}_6$, and $\text{Co}_{10}\text{Zn}_{10}$. With a focused laser, we explored the magnetization dynamics at different positions on the thin films. We report on the $\text{Co}_8\text{Zn}_8\text{Mn}_4$ sample which exhibited the spin-wave spectra plotted in Figure 6e–g. Here, we explore the thermally excited spin waves. In Figure 6e, we observe a broad peak shifting from about 3 GHz at low magnetic field to 11 GHz at 250 mT. The intensity (line width) of the main peak decreases (increases) with increasing field suggestive of appreciable Gilbert damping.⁴⁴ To determine the possible spatial variation of the properties, we have taken successive spectra along two neighboring line of 500 nm length (see Figure S4 in Supporting Information). Depending on the exact position, the broad peak indicated two nearby resonances, whose relative intensities varied along the scan. A spectrum taken at 90 mT with a large signal-to-noise ratio is depicted in Figure 6f. The data could be fitted with three bands at 4.1, 5.9, and 7.0 GHz of different intensity. The fit is displayed by the green solid line. Three resonances would be consistent with a skyrmion lattice supporting one breathing and two gyroscopic modes.⁴⁵ To further investigate the role of the microstructure for the spectra, we performed BLS in areas with different morphology. Columns, granular, and merged morphologies were first identified by AFM maps. BLS measurements were then subsequently performed in the selected regions (Figure S5 in Supporting Information) such that individual spectra were attributed to these three different morphologies. The corresponding measurements are shown in Figure 6g. BLS spectra of columns, granular, and merged films are plotted, respectively, in

yellow, blue and red. All three regions show a prominent peak of thermally excited spin waves at almost the same frequency (7.3 ± 0.2 GHz). This observation suggests that the regions exhibited similar values of saturation magnetization and internal field.⁴⁴ Spectra attributed to the granular film region (bottom curve) show a line width of the main peak of 2.2 ± 0.1 GHz compared to 3.1 ± 0.3 GHz for the two other morphologies. Further temperature dependent BLS measurements would be needed to explore the spin-wave resonances across the full magnetic phase diagram and develop a microscopic understanding of the morphology-dependent inhomogeneous broadening. Such experiments are beyond the scope of this paper, reporting on vdW growth of CoZnMn alloys on graphene on SiO₂/Si substrates.

CONCLUSIONS

In summary, we demonstrated vdWE of the MBE grown metallic Co_{10-x}Zn_{10-y}Mn_{x+y} thin films on graphene on oxidized silicon. We studied growth conditions as a function of substrate temperature and growth rate to control the morphology, crystal phase, and stoichiometry. SEM time series show the evolution of the morphology from islands to columns and merged films in association with the graphene quality. The substrate temperature series suggests that more pronounced facets of crystals occur for lower *T*, as low as 180 °C. The cross-sectional TEM and SAED confirm material crystallinity and further show structural quality improvement as islands evolve into columns and merged films. High-quality vdWE growth is proved from TEM on Co₈Zn₈Mn₄ since no misfit dislocations were observed. EDS suggests strong composition dependence on the substrate coverage attributed to relatively low Zn adsorption coefficient with respect to Mn and Co. Magnetic properties measured using SQUID give a quantitative comparison between thin film and bulk for different stoichiometry $0 < x, y < 3$. ACMS and BLS results suggest a phase transition at room temperature in Co₈Zn₈Mn₄. Combined together, these results open the door toward the growth of fully relaxed and high-quality Co–Zn–Mn thin films on any substrate, and provide a promising path for skyrmionic device integration.

ASSOCIATED CONTENT

Supporting Information

The Supporting Information is available free of charge at <https://pubs.acs.org/doi/10.1021/acs.jpcc.1c00452>.

Raman spectra of monolayer graphene on SiO₂(300 nm)/Si (Figure S1); HRTEM of Co₈Zn₈Mn₄ lamella (Figure S2); SAED micrographs and pattern simulation (Figure S3); space resolved BLS measurements performed on Co₈Zn₈Mn₄ at 90 mT (Figure S4); and detailed AFM investigations of Co₈Zn₈Mn₄ to identify three regions of different morphology (Figure S5) (PDF)

AUTHOR INFORMATION

Corresponding Authors

Anna Kúkolová – Laboratory of Semiconductor Materials, Institute of Materials, Ecole Polytechnique Fédérale de Lausanne EPFL, Lausanne 1015, Switzerland; Laboratory of Nanoscale Magnetic Materials and Magnonics, Institute of Materials, Ecole Polytechnique Fédérale de Lausanne EPFL, Lausanne 1015, Switzerland; orcid.org/0000-0002-3377-7647; Email: anna.kukolova@epfl.ch

Dirk Grundler – Laboratory of Nanoscale Magnetic Materials and Magnonics, Institute of Materials, Ecole Polytechnique Fédérale de Lausanne EPFL, Lausanne 1015, Switzerland; Institute of Microengineering, Ecole Polytechnique Fédérale de Lausanne EPFL, Lausanne 1015, Switzerland; orcid.org/0000-0002-4966-9712; Email: dirk.grundler@epfl.ch

Anna Fontcuberta i Morral – Laboratory of Semiconductor Materials, Institute of Materials, Ecole Polytechnique Fédérale de Lausanne EPFL, Lausanne 1015, Switzerland; Institute of Physics, Faculty of Basic Sciences, Ecole Polytechnique Fédérale de Lausanne EPFL, Lausanne 1015, Switzerland; orcid.org/0000-0002-5070-2196; Email: anna.fontcuberta-morral@epfl.ch

Authors

Simon Escobar Steinvall – Laboratory of Semiconductor Materials, Institute of Materials, Ecole Polytechnique Fédérale de Lausanne EPFL, Lausanne 1015, Switzerland

Rajrupa Paul – Laboratory of Semiconductor Materials, Institute of Materials, Ecole Polytechnique Fédérale de Lausanne EPFL, Lausanne 1015, Switzerland; orcid.org/0000-0002-7532-5593

Jean-Baptiste Leran – Laboratory of Semiconductor Materials, Institute of Materials, Ecole Polytechnique Fédérale de Lausanne EPFL, Lausanne 1015, Switzerland

Ping Che – Laboratory of Nanoscale Magnetic Materials and Magnonics, Institute of Materials, Ecole Polytechnique Fédérale de Lausanne EPFL, Lausanne 1015, Switzerland

Mohammad Hamdi – Laboratory of Nanoscale Magnetic Materials and Magnonics, Institute of Materials, Ecole Polytechnique Fédérale de Lausanne EPFL, Lausanne 1015, Switzerland

Andrea Mucchietto – Laboratory of Nanoscale Magnetic Materials and Magnonics, Institute of Materials, Ecole Polytechnique Fédérale de Lausanne EPFL, Lausanne 1015, Switzerland

Complete contact information is available at: <https://pubs.acs.org/doi/10.1021/acs.jpcc.1c00452>

Notes

The authors declare no competing financial interest.

ACKNOWLEDGMENTS

The authors thank SNF for the financial support via sinergia project 171003 (Nanoskyrmionics) and projects BSCGIO-157705 and 177550.

ADDITIONAL NOTE

^aSubstrate temperature is the nominal temperature of the heater situated in proximity of the substrate.

REFERENCES

- (1) Mühlbauer, S.; Binz, B.; Jonietz, F.; Pfleiderer, C.; Rosch, A.; Neubauer, A.; Georgii, R.; Böni, P. Skyrmion lattice in a chiral magnet. *Science* **2009**, *323*, 915–919.
- (2) Neubauer, A.; Pfleiderer, C.; Binz, B.; Rosch, A.; Ritz, R.; Niklowitz, P. G.; Böni, P. Topological hall effect in the a phase of MnSi. *Phys. Rev. Lett.* **2009**, *102*, 186602.
- (3) Adams, T.; Mühlbauer, S.; Pfleiderer, C.; Jonietz, F.; Bauer, A.; Neubauer, A.; Georgii, R.; Böni, P.; Keiderling, U.; Everschor, K.; et al. Long-range crystalline nature of the Skyrmion lattice in MnSi. *Phys. Rev. Lett.* **2011**, *107*, 217206.

- (4) Mühlbauer, S.; Kindervater, J.; Adams, T.; Bauer, A.; Keiderling, U.; Pfleiderer, C. Kinetic small angle neutron scattering of the skyrmion lattice in MnSi. *New J. Phys.* **2016**, *18*, 075017.
- (5) Huang, S. X.; Chien, C. L. Extended skyrmion phase in epitaxial FeGe(111) thin films. *Phys. Rev. Lett.* **2012**, *108*, 267201.
- (6) Yu, X. Z.; Kanazawa, N.; Onose, Y.; Kimoto, K.; Zhang, W. Z.; Ishiwata, S.; Matsui, Y.; Tokura, Y. Near room-temperature formation of a skyrmion crystal in thin-films of the helimagnet FeGe. *Nat. Mater.* **2011**, *10*, 106–109.
- (7) Seki, S.; Yu, X. Z.; Ishiwata, S.; Tokura, Y. Observation of skyrmions in a multiferroic material. *Science* **2012**, *336*, 198–201.
- (8) Tokunaga, Y.; Yu, X. Z.; White, J. S.; Rønnow, H. M.; Morikawa, D.; Taguchi, Y.; Tokura, Y. A new class of chiral Mater. hosting magnetic skyrmions beyond room temperature. *Nat. Commun.* **2015**, *6*, 7638.
- (9) Tonomura, A.; Yu, X.; Yanagisawa, K.; Matsuda, T.; Onose, Y.; Kanazawa, N.; Park, H. S.; Tokura, Y. Real-space observation of skyrmion lattice in helimagnet MnSi thin samples. *Nano Lett.* **2012**, *12*, 1673–1677.
- (10) Nagase, T.; Komatsu, M.; So, Y. G.; Ishida, T.; Yoshida, H.; Kawaguchi, Y.; Tanaka, Y.; Saitoh, K.; Ikarashi, N.; Kuwahara, M.; et al. Smectic Liquid-Crystalline Structure of Skyrmions in Chiral Magnet $\text{Co}_{0.8}\text{Zn}_{0.7}\text{Mn}_4(110)$ Thin Film. *Phys. Rev. Lett.* **2019**, *123*, 137203.
- (11) Wilson, M. N.; Karhu, E. A.; Quigley, A. S.; Rößler, U. K.; Butenko, A. B.; Bogdanov, A. N.; Robertson, M. D.; Monchesky, T. L. Extended elliptic skyrmion gratings in epitaxial MnSi thin films. *Phys. Rev. B: Condens. Matter Mater. Phys.* **2012**, *86*, 144420.
- (12) Yokouchi, T.; Kanazawa, N.; Tsukazaki, A.; Kozuka, Y.; Kawasaki, M.; Ichikawa, M.; Kagawa, F.; Tokura, Y. Stability of two-dimensional skyrmions in thin films of $\text{Mn}_{1-x}\text{Fe}_x\text{Si}$ investigated by the topological Hall effect. *Phys. Rev. B: Condens. Matter Mater. Phys.* **2014**, *89*, 064416.
- (13) Gallagher, J. C.; Meng, K. Y.; Brangham, J. T.; Wang, H. L.; Esser, B. D.; McComb, D. W.; Yang, F. Y. Robust Zero-Field Skyrmion Formation in FeGe Epitaxial Thin Films. *Phys. Rev. Lett.* **2017**, *118*, 027201.
- (14) Mathur, N.; Stolt, M. J.; Niitsu, K.; Yu, X.; Shindo, D.; Tokura, Y.; Jin, S. Electron Holography and Magnetotransport Measurements Reveal Stabilized Magnetic Skyrmions in $\text{Fe}_{1-x}\text{Co}_x\text{Si}$ Nanowires. *ACS Nano* **2019**, *13*, 7833–7841.
- (15) Yu, X.; Degraeve, J. P.; Hara, Y.; Hara, T.; Jin, S.; Tokura, Y. Observation of the magnetic skyrmion lattice in a MnSi nanowire by Lorentz TEM. *Nano Lett.* **2013**, *13*, 3755–3759.
- (16) Sinha, P.; Porter, N. A.; Marrows, C. H. Strain-induced effects on the magnetic and electronic properties of epitaxial $\text{Fe}_{1-x}\text{Co}_x\text{Si}$ thin films. *Phys. Rev. B: Condens. Matter Mater. Phys.* **2014**, *89*, 134426.
- (17) Meynell, S. A.; Wilson, M. N.; Loudon, J. C.; Spitzig, A.; Rybakov, F. N.; Johnson, M. B.; Monchesky, T. L. Hall effect and transmission electron microscopy of epitaxial MnSi thin films. *Phys. Rev. B: Condens. Matter Mater. Phys.* **2014**, *90*, 224419.
- (18) Bocarsly, J. D.; Heikes, C.; Brown, C. M.; Wilson, S. D.; Seshadri, R. Deciphering structural and magnetic disorder in the chiral skyrmion host Mater. $\text{Co}_x\text{Zn}_y\text{Mn}_z$ ($x+y+z = 20$). *Phys. Rev. Mater.* **2019**, *3*, 014402.
- (19) Nakajima, T.; Karube, K.; Ishikawa, Y.; Yonemura, M.; Reynolds, N.; White, J. S.; Rønnow, H. M.; Kikkawa, A.; Tokunaga, Y.; Taguchi, Y.; et al. Correlation between site occupancies and spin-glass transition in skyrmion host. *Phys. Rev. B: Condens. Matter Mater. Phys.* **2019**, *100*, 064407.
- (20) Karube, K.; Shibata, K.; White, J. S.; Koretsune, T.; Yu, X. Z.; Tokunaga, Y.; Rønnow, H. M.; Arita, R.; Arima, T.; Tokura, Y.; et al. Controlling the helicity of magnetic skyrmions in a β -Mn-type high-temperature chiral magnet. *Phys. Rev. B: Condens. Matter Mater. Phys.* **2018**, *98*, 155120.
- (21) Koma, A.; Yoshimura, K. Ultrasharp interfaces grown with Van der Waals epitaxy. *Surf. Sci.* **1986**, *174*, 556–560.
- (22) Utama, M. I. B.; Zhang, Q.; Zhang, J.; Yuan, Y.; Belarre, F. J.; Arbiol, J.; Xiong, Q. Recent developments and future directions in the growth of nanostructures by van der Waals epitaxy. *Nanoscale* **2013**, *5*, 3570–3588.
- (23) Zhou, X.; Brzostowski, B.; Durajski, A.; Liu, M.; Xiang, J.; Jiang, T.; Wang, Z.; Chen, S.; Li, P.; Zhong, Z.; et al. Atomically Thin 1T- FeCl_2 Grown by Molecular-Beam Epitaxy. *J. Phys. Chem. C* **2020**, *124*, 9416–9423.
- (24) Dai, L.; Niu, G.; Zhao, J.; Zhao, H.; Liu, Y.; Wang, Y.; Zhang, Y.; Wu, H.; Wang, L.; Pfützenreuter, D.; et al. Toward van der Waals epitaxy of transferable ferroelectric barium titanate films: Via a graphene monolayer. *J. Mater. Chem. C* **2020**, *8*, 3445–3451.
- (25) Shibata, T.; Takano, H.; Ebina, Y.; Kim, D. S.; Ozawa, T. C.; Akatsuka, K.; Ohnishi, T.; Takada, K.; Kogure, T.; Sasaki, T. Versatile van der Waals epitaxy-like growth of crystal films using two-dimensional nanosheets as a seed layer: Orientation tuning of SrTiO₃ films along three important axes on glass substrates. *J. Mater. Chem. C* **2014**, *2*, 441–449.
- (26) Nakada, K.; Ishii, A. Migration of adatom adsorption on graphene using DFT calculation. *Solid State Commun.* **2011**, *151*, 13–16.
- (27) Lin, Y. C.; Lu, N.; Perea-Lopez, N.; Li, J.; Lin, Z.; Peng, X.; Lee, C. H.; Sun, C.; Calderin, L.; Browning, P. N.; et al. Direct synthesis of van der Waals solids. *ACS Nano* **2014**, *8*, 3715–3723.
- (28) Okamoto, H. Co-Zn (Cobalt-Zinc). *J. Phase Equilib. Diffus.* **2006**, *27*, 311.
- (29) Okamoto, H.; Tanner, L. E. The Mn-Zn (Manganese-Zinc) system. *Bull. Alloy Phase Diagrams* **1990**, *11*, 377–384.
- (30) Ishida, K.; Nishizawa, T. The Co-Mn (Cobalt-Manganese) system. *Bull. Alloy Phase Diagrams* **1990**, *11*, 125–137.
- (31) Zhou, H.; Qiu, C.; Liu, Z.; Yang, H.; Hu, L.; Liu, J.; Yang, H.; Gu, C.; Sun, L. Thickness-dependent morphologies of gold on N-layer graphenes. *J. Am. Chem. Soc.* **2010**, *132*, 944–946.
- (32) Zhou, H. Q.; Yu, F.; Yang, H. C.; Chen, M. J.; Wang, G.; Sun, L. F. High-throughput thickness determination of n-layer graphenes via gold deposition. *Chem. Phys. Lett.* **2011**, *518*, 76–80.
- (33) Gao, T.; Gao, Y.; Chang, C.; Chen, Y.; Liu, M.; Xie, S.; He, K.; Ma, X.; Zhang, Y.; Liu, Z. Atomic-scale morphology and electronic structure of manganese atomic layers underneath epitaxial graphene on SiC(0001). *ACS Nano* **2012**, *6*, 6562–6568.
- (34) Poon, S. W.; Wee, A. T.; Tok, E. S. Anomalous scaling behaviour of cobalt cluster size distributions on graphite, epitaxial graphene and carbon-rich R30°. *Surf. Sci.* **2012**, *606*, 1586–1593.
- (35) Binz, S. M.; Hupaló, M.; Liu, X.; Wang, C. Z.; Lu, W. C.; Thiel, P. A.; Ho, K. M.; Conrad, E. H.; Tringides, M. C. High island densities and long range repulsive interactions: Fe on epitaxial graphene. *Phys. Rev. Lett.* **2012**, *109*, 026103.
- (36) Evans, J. W.; Thiel, P. A.; Bartelt, M. C. Morphological evolution during epitaxial thin film growth: Formation of 2D islands and 3D mounds. *Surf. Sci. Rep.* **2006**, *61*, 1–128.
- (37) Paul, R.; Humblot, N.; Steinvall, S. E.; Stutz, E. Z.; Joglekar, S. S.; Leran, J. B.; Zamani, M.; Cayron, C.; Logé, R.; Aguila, A. G. D.; et al. Van der Waals Epitaxy of Earth-Abundant Zn₃P₂ on Graphene for Photovoltaics. *Cryst. Growth Des.* **2020**, *20*, 3816–3825.
- (38) Menzel, D.; Baabe, D.; Litterst, F. J.; Steinki, N.; Dietze, K.; Sach, M.; Rubrecht, B.; Süllow, S.; Hoser, A. Local structure determination in helimagnetic Local structure determination in helimagnetic $\text{Co}_8\text{Zn}_8\text{Mn}_{4-x}\text{Fe}_x$. *J. Phys. Commun.* **2019**, *3*, 25001.
- (39) Karube, K.; White, J. S.; Reynolds, N.; Gavilano, J. L.; Oike, H.; Kikkawa, A.; Kagawa, F.; Tokunaga, Y.; Rønnow, H. M.; Tokura, Y.; et al. Robust metastable skyrmions and their triangular-square lattice structural transition in a high-temperature chiral magnet. *Nat. Mater.* **2016**, *15*, 1237–1242.
- (40) Nakamura, H.; Yoshimoto, K.; Shiga, M.; Nishi, M.; Kakurai, K. Strong antiferromagnetic spin fluctuations and the quantum spin-liquid state in geometrically frustrated β -Mn, and the transition to a spin-glass state caused by non-magnetic impurity. *J. Phys.: Condens. Matter* **1997**, *9*, 4701–4728.
- (41) Stewart, J. R.; Cywinski, R. Magnetic short-range order in β - $\text{Mn}_{1-x}\text{Co}_x$. *J. Phys.: Condens. Matter* **2009**, *21*, 6.

(42) Karube, K.; White, J. S.; Morikawa, D.; Dewhurst, C. D.; Cubitt, R.; Kikkawa, A.; Yu, X.; Tokunaga, Y.; Arima, T.-h.; Rønnow, H. M.; et al. Disordered skyrmion phase stabilized by magnetic frustration in a chiral magnet. *Sci. Adv.* **2018**, *4*, No. eaar7043.

(43) Karube, K.; White, J. S.; Ukleev, V.; Dewhurst, C. D.; Cubitt, R.; Kikkawa, A.; Tokunaga, Y.; Rønnow, H. M.; Tokura, Y.; Taguchi, Y. Metastable skyrmion lattices governed by magnetic disorder and anisotropy in β -Mn-type chiral magnets. *Phys. Rev. B: Condens. Matter Mater. Phys.* **2020**, *102*, 064408.

(44) Gurevich, A. G.; Melkov, G. A. *Magnetization Oscillations and Waves*; CRC Press, Inc.: FL, 1996.

(45) Schwarze, T.; Waizner, J.; Garst, M.; Bauer, A.; Stasinopoulos, L.; Berger, H.; Pfleiderer, C.; Grundler, D. Universal helimagnon and skyrmion excitations in metallic, semiconducting and insulating chiral magnets. *Nat. Mater.* **2015**, *14*, 478–483.